

# Revisiting dense granular flow dynamics: Compressibility and nonlocality on inclined surfaces

You-Yu Chang<sup>1,\*</sup> and Fu-Ling Yang<sup>1,\*\*</sup>

<sup>1</sup>Department of Mechanical Engineering, National Taiwan University, Taipei 106319, Taiwan

**Abstract.** This study presents a compressible nonlocal continuum model for two-dimensional granular flows on inclined surfaces. We derive analytical solutions for the solid volume fraction,  $\phi(y^*)$ , and the streamwise velocity profile,  $u^*(y^*)$ , by employing the method of matched asymptotic expansions. The inner solution for  $\phi(y^*)$  is found to be constant at the maximum packing fraction, while the outer solution exhibits a linear decrease, with the matching point determined by mass conservation. Furthermore, we obtain an analytic non-Bagnold  $u^*(y^*)$  that can transit smoothly from the no-slip condition at the rough base to the strain-free condition at the free surface. Not only are the continuity conditions of velocity and shear rate invoked at the matching point, but the continuity of shear work is also introduced as a novel condition. In addition, fitting curves are established for the densest packing volume fraction,  $\phi_{max}(\theta)$ , and the mean volume fraction,  $\bar{\phi}(\theta)$ , based on experimental data, highlighting their dependence on the inclination angle  $\theta$ . Notably, we reveal that a dimensionless parameter  $\eta$  appears solely in the governing equations of  $u^*(y^*)$ . Furthermore, at  $\eta \approx 7.3$ , a balance is achieved between compressibility and nonlocality.

## 1 Introduction

The continuum-mechanical description of granular flows has attracted attention for modeling both industrial and geophysical processes. Because granular bulk motion begins only when a critical yield stress is reached within the packing, these flows are divided into three regimes: a solid-like quasistatic regime with slow bulk deformation and frictional contacts; a gas-like inertial regime where high flow speeds and repulsive collisions dominate; and an intermediate liquid-like regime in which dense material flows due to simultaneous collision and friction interactions [1].

Researchers have developed phenomenological local constitutive models for dense granular flows of rigid grains. Shear stress  $\|\tau\|$  is described in proportion to isotropic pressure  $p$  by  $\|\tau\| = \mu(I)p$ , where the effective friction coefficient,  $\mu(I)$ , depends on the dimensionless inertial number  $I$  [2, 3]. However, on inclined surfaces, thin granular layers require a greater inclination angle  $\theta$  to initiate flow, indicating a thickness-dependent internal strength  $\mu_s$  [4]. Furthermore, in the quasistatic regime, the stress is found independent of the shear rate, challenging the assumed colinearity between the shear stress and the shear rate tensors [5, 6]. To overcome these limitations, various nonlocal models invoking different physical processes have been proposed [7–9]. Although continuum and discrete simulations based on these models successfully capture flow dynamics [10], they typically assume that the granular medium is incompressible.

However, the effect of dilatancy on particle rearrangement and bulk deformation is a well-known phenomenon, suggesting local compressibility and its impact on solid volume fraction  $\phi$ . Several local dilatancy laws have been proposed to describe these variations [2, 11]. Dsouza and Nott applied the critical state theory and the extended von Mises condition to develop a nonlocal rheology model using a volume-averaged approach [12]. To our best knowledge, this remains the only framework that simultaneously ensures kinematic determinacy and accounts for dilatancy in dense granular flows. The equations are given by

$$\boldsymbol{\sigma} = -p\boldsymbol{\delta} + \frac{2\mu_s}{\dot{\gamma}} (p_c \mathbf{D} - \ell^2 \Pi \nabla^2 \mathbf{D}), \quad (1a)$$

$$p_c = \Pi - \ell^2 \frac{d\Pi}{d\phi} \nabla^2 \phi, \quad (1b)$$

$$p = p_c \left( 1 - \frac{n-1}{n\mu_s \dot{\gamma}} \nabla \cdot \mathbf{u} \right) + \ell^2 \Pi \frac{n-1}{n\mu_s \dot{\gamma}} \nabla^2 (\nabla \cdot \mathbf{u}), \quad (1c)$$

where the  $\ell^2$ -order terms represent nonlocal modifications. Here,  $\boldsymbol{\delta}$  is the identity matrix,  $\mathbf{u} = (u, v)$  is the velocity vector,  $\mathbf{D}$  is the deviatoric deformation rate tensor with magnitude  $\dot{\gamma} = \sqrt{2\mathbf{D} : \mathbf{D}}$ ,  $p_c$  is the critical state pressure,  $\ell$  is the effective radius measuring nonlocal effect,  $n \gtrsim 1$  determines yield surface convexity, and  $\Pi$  is the local critical state pressure proposed to be

$$\Pi(\phi) = \alpha \frac{(\phi - \phi_{min})^2}{(\phi_{max} - \phi)^5}, \quad (2)$$

where  $\alpha \sim 0.5$  is a material constant,  $\phi_{min}$  and  $\phi_{max}$  are the volume fractions for the loosest and the densest packing, respectively [13].

\*e-mail: f09522109@ntu.edu.tw

\*\*e-mail: fulingyang@ntu.edu.tw

In this work, the two-dimensional version of this non-local compressible flow model is solved for steady inclined surface granular flows. By imposing conventional boundary conditions on the volume fraction and stream-wise velocity, we analytically solve their depth profiles using matched asymptotic analysis. Our results reproduce the observed evolution of the velocity profile, from concave to S-shaped, as the flow becomes denser, consistent with the findings from discrete element simulations [4].

## 2 Problem formulation

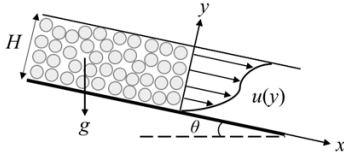


**Figure 1.** Schematic diagram of inclined surface granular flows.

Consider a steady two-dimensional compressible granular flow of constant height  $H$  with grain density  $\rho_s$  down a rough incline at angle  $\theta$ , as shown in figure 1. The flow satisfies mass and linear momentum conservation

$$\nabla \cdot (\phi \mathbf{u}) = 0, \quad (3a)$$

$$\rho_s \phi \mathbf{u} \cdot \nabla \mathbf{u} = \nabla \cdot \boldsymbol{\sigma} + \rho_s \phi \mathbf{g}. \quad (3b)$$

Here,  $\mathbf{g} = (g \sin \theta, -g \cos \theta)$  is the gravitational acceleration vector, and the Cauchy stress tensor  $\boldsymbol{\sigma}$  is assumed symmetric to satisfy angular momentum conservation.

For a fully-developed flow, (3a) simplifies to  $\phi v = 0$ , leading to  $v = 0$  with the impermeable basal condition. The relevant momentum equations then reduce to  $d\sigma_{yy}/dy - \rho_s \phi g \cos \theta = 0$  and  $d\sigma_{yx}/dy + \rho_s \phi g \sin \theta = 0$ . Substituting (1a)-(1c) and (2) into these equations yields the nonlocal governing equations for  $\phi$  and  $u$  as

$$\frac{dp_c^*}{dy^*} = -\phi, \quad (4a)$$

$$\frac{d}{dy^*} \left( \mu_s p_c^* - \ell^{*2} \mu_s \alpha^* \frac{\phi^2}{(\phi_{max} - \phi)^5} \frac{d^3 u^*}{dy^{*3}} \right) = -\phi \tan \theta. \quad (4b)$$

As we are dealing with inclined surface flows, we set  $\phi_{min} \sim 0$  as the reported surface volume fraction [4, 14], which is much lower than the conventional  $\phi_{min} \sim 0.5$  for simple shear flows. The variables are nondimensionalized as  $y^* = y/H$ ,  $\ell^* = \ell/H$ ,  $u^* = u/\sqrt{gH \cos \theta}$ ,  $p_c^* = p_c/\rho_s g H \cos \theta$ , and  $\alpha^* = \alpha/\rho_s g H \cos \theta$ . Note that we scale out the dependence of  $\cos \theta$  as it remains of order unity for flows down milder slopes and preserves the nature of (4b) [15]. The effect of the inclination angle remains in the term  $-\phi \tan \theta$  in (4b).

## 3 Matched asymptotic expansions of $\phi(y^*)$

Since (4a) coupled with (1b) and (2) is highly nonlinear, we employ matched asymptotic expansions to obtain the

volume fraction profile  $\phi(y^*)$ . For small  $y^*$  near the base, we expect that the value of  $\phi(y^*)$  remains nearly constant to assume  $d\phi/dy^* \approx d^2\phi/dy^{*2} \approx d^3\phi/dy^{*3} \approx \varepsilon$  [4, 16]. Keeping only the leading order terms yields the governing equation for the inner solution as

$$\phi_I(\phi_{max} - \phi_I)^7 = 0. \quad (5)$$

The nontrivial solution of (5) is  $\phi_I(y^*) = \phi_{max}$ . Conversely,  $\phi(y^*)$  tends to zero near the free surface as suggested in the literature [14]. Setting  $\phi \approx \varepsilon$  in (4a) and performing an order analysis leads to the governing equation for the outer solution as

$$2\ell^{*2} \alpha^* (\phi_{max} - \phi_O)^2 \frac{d\phi_O}{dy^*} \frac{d^2\phi_O}{dy^{*2}} = 0. \quad (6)$$

The general solution of  $\phi_O(y^*)$  is obviously a linear function, involving two undetermined coefficients.

We then enforce two natural boundary conditions used in the previous paragraph:  $d\phi_I/dy^*(y^* = 0) = 0$  and  $\phi_O(y^* = 1) = 0$ . Continuity of  $\phi(y^*)$  requires  $\phi_I(y^* = y_m^*) = \phi_O(y^* = y_m^*)$ , where  $y_m^*$  is the matching point. We may impose an overall mass conservation  $\int_0^1 \phi(y^*) dy^* = \bar{\phi}$  with a specified mean volume fraction  $\bar{\phi}$ . This leads to

$$y_m^* = \frac{2\bar{\phi} - \phi_{max}}{\phi_{max}}, \quad (7a)$$

$$\phi_I(y^*) = \phi_{max}, y^* \leq y_m^*, \quad (7b)$$

$$\phi_O(y^*) = \frac{1}{2} \frac{\phi_{max}^2}{\phi_{max} - \bar{\phi}} (1 - y^*), y^* > y_m^*. \quad (7c)$$

If  $\bar{\phi} = \phi_{max}$ , we find  $y_m^* = 1$  and  $\phi(y^*) = \phi_{max}$ , indicating incompressible flow as a special case.

To achieve flow prediction with (7), we must provide  $\phi_{max}$  and  $\bar{\phi}$  for a specific flow condition. As noted in the literature, both  $\phi_{max}$  and  $\bar{\phi}$  are independent of the flow height  $H$  but decrease with increasing  $\theta$  [16]. Hence, we consult to the literature to fit [17]

$$\phi_{max}(\theta) = -0.3929 \tan \theta + 0.9356, \quad (8a)$$

$$\bar{\phi}(\theta) = -0.5329 \tan \theta + 0.9813. \quad (8b)$$

We choose to use  $\tan \theta$  as it represents both the surface slope and the local effective friction coefficient. The clean trends with the coefficient of determination ( $R^2$ ) are shown in figures 2 and 3.

To validate (7a)-(7c), the nonlinear equation (4a)-(1b)-(2) is solved by `scipy.integrate.solve_bvp` with 1000 grid points over  $y^* \in [0, 1]$  and an initial guess of  $\phi(y^*) = \bar{\phi}$ . The boundary conditions  $d\phi/dy^*(y^* = 0) = 0$  and  $\phi(y^* = 1) = 0$  are enforced, while  $\phi(y^* = 0)$  is iteratively adjusted to satisfy the convergence criterion  $\int_0^1 \phi(y^*) dy^* - \bar{\phi} < 10^{-3}$ . We compare the analytical and numerical solutions in figures 4 and 5 at  $\theta = 15^\circ, 20^\circ, 25^\circ, 30^\circ$  by their  $L^2$  relative error norms, which are as small as 0.04, 0.02, 0.02, 0.02, respectively. The results show minor yet consistent deviations near the matching points. These discrepancies arise as the matching conditions at the inner-outer transition do not enforce derivative continuity, leading to a nonsmooth, edge-like local profile in the analytical solutions. Such a sharp decay near the free surface is also reported from DEM simulations [4].

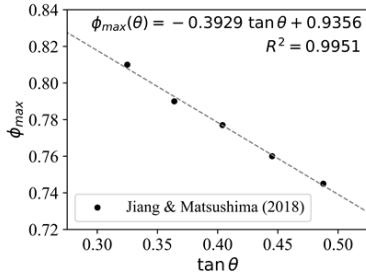


**Figure 2.** Simulation data of  $\phi_{max}$  versus inclination angle  $\theta$  [17].

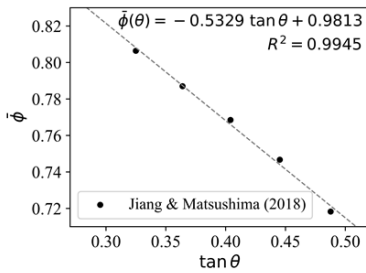


**Figure 3.** Simulation data of  $\bar{\phi}$  versus inclination angle  $\theta$  [17].

#### 4 Matched asymptotic expansions of $u^*(y^*)$

Similarly, we employ asymptotic analysis to determine the streamwise velocity profile  $u^*(y^*)$ , as the governing equation (4b) is also highly nonlinear. For small  $y^*$ , we adopt the same assumption as in the previous section and further approximate  $\phi(y^*) - \phi_{max} \approx \varepsilon$  based on (7b). Substituting these scaling relations into (4b) and retaining only the leading order terms, we obtain the governing equation for the inner solution as

$$\frac{du_I^*}{dy^*} \frac{d^4 u_I^*}{dy^{*4}} - \frac{d^2 u_I^*}{dy^{*2}} \frac{d^3 u_I^*}{dy^{*3}} + 5 \frac{du_I^*}{dy^*} \frac{d^3 u_I^*}{dy^{*3}} = 0. \quad (9)$$

Around the free surface where  $\phi(y^*)$  approaches zero, we set  $\phi \approx \varepsilon$  in (4b) and perform an order analysis to find the governing equation of outer solution as

$$\frac{d^3 u_O^*}{dy^{*3}} + \eta^2 \frac{du_O^*}{dy^*} = 0, \quad (10a)$$

$$\eta = \sqrt{\frac{(\tan \theta - \mu) \phi_{max}^3(\theta) [\phi_{max}(\theta) - \bar{\phi}(\theta)]}{\mu \ell^{*2} \alpha^*}}, \quad (10b)$$

with a newly discovered parameter in (10b) that seems to embed most of the flow controlling variables. The physical meaning of this parameter is beyond the scope of this work and will be pursued in future work.

At the rough base, we impose a no-slip boundary condition  $u_I^*(y^* = 0) = 0$ , and a finite shear rate  $du_I^*/dy^*(y^* = 0) = \dot{\gamma}_b^*$ , as reported in the literature [4, 16]. At the free surface, we enforce the strain-free condition  $du_O^*/dy^*(y^* = 1) = 0$ , along with a finite variation,  $d^2 u_O^*/dy^{*2}(y^* = 1) = \dot{\gamma}_s^{*'}$ , since the strain rate does not always level off, especially in slow and thick flows [18, 19]. Furthermore,  $u^*(y^*)$

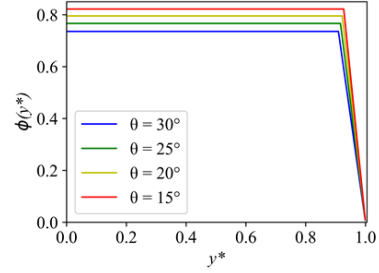


**Figure 4.** Analytical solutions of  $\phi(y^*)$  at  $\theta = 15^\circ, 20^\circ, 25^\circ, 30^\circ$ .

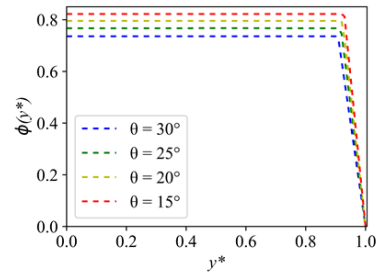


**Figure 5.** Numerical solutions of  $\phi(y^*)$  at  $\theta = 15^\circ, 20^\circ, 25^\circ, 30^\circ$ .

and  $du^*/dy^*$  must be continuous at the matching point, requiring  $u_I^* = u_O^*$  and  $du_I^*/dy^* = du_O^*/dy^*$  when  $y^* = y_m^*$ . Additionally, by incorporating the energy equation [20], we further require that the shear work must also remain continuous at the matching point,

$$\left( \frac{d\phi_I}{dy^*} \frac{du_I^*}{dy^*} - \phi_I \frac{d^2 u_I^*}{dy^{*2}} = \frac{d\phi_O}{dy^*} \frac{du_O^*}{dy^*} - \phi_O \frac{d^2 u_O^*}{dy^{*2}} \right)_{y^*=y_m^*}. \quad (11)$$

Using these conditions, the  $u^*(y^*)$  profile can be solved as

$$u_i^*(y^*) = G_{1.3}^{2.0} \left( -\frac{C^2 e^{-5y^*}}{4} \middle| \begin{matrix} 1 \\ 0, 0, 0 \end{matrix} \right) + G_{1.3}^{3.0} \left( \frac{C e^{-\frac{5}{2}y^*}}{2}, \frac{1}{2} \middle| \begin{matrix} 1 \\ 0, 0, 0 \end{matrix} \right), \quad (12a)$$

$$u_o^*(y^*) = u_i^*(y_m^*) + \frac{\dot{\gamma}_s^{*'}}{\eta} \{ \cos[\sqrt{\eta}(1 - y^*)] - \cos[\sqrt{\eta}(1 - y_m^*)] \}. \quad (12b)$$

Note that  $G_{p,q}^{m,n}(x|\cdot)$  and  $G_{p,q}^{m,n}(x, r|\cdot)$  denote the Meijer G-function and the generalized Meijer G-function, respectively. The unknown coefficient  $C$  in (12a) cannot be explicitly solved but subjected to an implicit relation

$$\frac{\dot{\gamma}_b^*}{\dot{\gamma}_s^{*'}} = \frac{\left\{ \begin{array}{l} -5C^* \sin[\eta(1 - y_m^*)] [I_1(C^*)K_0(C) + I_0(C)K_1(C^*)] \\ -\frac{2}{1 - y_m^*} \sin[\eta(1 - y_m^*)] [I_0(C^*)K_0(C) - I_0(C)K_0(C^*)] \\ + 2\eta \cos[\eta(1 - y_m^*)] [I_0(C^*)K_0(C) - I_0(C)K_0(C^*)] \end{array} \right\}}{5C^* \eta [I_0(C^*)K_1(C^*) + I_1(C^*)K_0(C^*)]}, \quad (13)$$

where  $C^* = C e^{-5y_m^*/2}$ . Clearly, the dimensionless parameter  $\eta$  in (10b) and the ratio between the boundary conditions have a strong influence on  $C$ . For very creeping flows, the base becomes non-shearing, with  $\dot{\gamma}_b^* \rightarrow 0$  and a negative  $\dot{\gamma}_s^{*'}$ , which implies  $\dot{\gamma}_b^*/\dot{\gamma}_s^{*'}$   $\rightarrow 0^-$ . In contrast,

the Bagnold velocity profile in the fast flow limit suggests  $\dot{\gamma}_s^{*'} \rightarrow 0^-$  and thus  $\dot{\gamma}_b^*/\dot{\gamma}_s^{*'} \rightarrow -\infty$ .

Once  $\theta$ ,  $\mu_s$ ,  $\alpha^*$ ,  $\ell^*$ , and  $\dot{\gamma}_b^*/\dot{\gamma}_s^{*'}$  are specified,  $C$  can be determined numerically, as shown in figure 6. Note that the inclination angles range from about  $12^\circ$  to  $36^\circ$  [16], we can consult to (7a) and (8) to find that  $y_m^*$  lies roughly between 0.90 and 0.93. At smaller  $\eta = 3$ ,  $y_m^*$  is positively correlated with  $C$  if  $\dot{\gamma}_b^*/\dot{\gamma}_s^{*'}$  is given. Conversely, at larger  $\eta = 9$ ,  $y_m^*$  is negatively correlated with  $C$  if  $\dot{\gamma}_b^*/\dot{\gamma}_s^{*'}$  is given. In particular, at  $\eta \approx 7.3$ , the value of  $C$  is independent of  $y_m^*$  and therefore  $\theta$ , indicating a balance between compressibility and nonlocal effect. This equilibrium suggests that  $\dot{\gamma}_b^*/\dot{\gamma}_s^{*'}$  depends only on  $C$  under such circumstances.

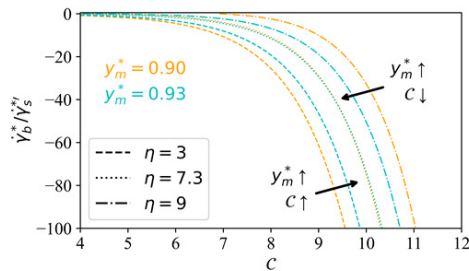


**Figure 6.** Functional relationships between  $\dot{\gamma}_b^*/\dot{\gamma}_s^{*'}$  and  $C$  with  $\eta = 3, 7.3, 9$  and  $y_m^* = 0.90, 0.93$ .

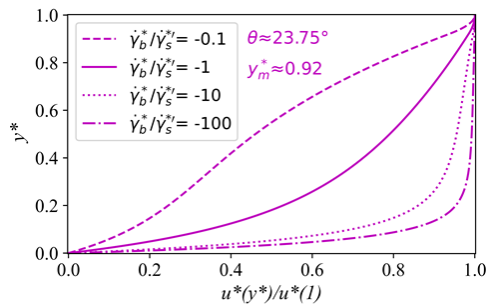


**Figure 7.** Normalized velocity profiles  $u^*(y^*)/u^*(1)$  with  $\dot{\gamma}_b^*/\dot{\gamma}_s^{*' = -0.1, -1, -10, -100$  with  $\theta \approx 23.75^\circ$  ( $y_m^* = 0.92$ ).

For example, with  $\theta \approx 23.75^\circ$  and  $\eta = 7.3$ , the velocity profiles for different  $\dot{\gamma}_b^*/\dot{\gamma}_s^{*' are shown in figure 7. When  $\dot{\gamma}_b^*/\dot{\gamma}_s^{*' = -0.1$ , we obtain the S-shaped velocity profile in the dense regime as reported from other nonlocal models [7, 9, 18]. As  $\dot{\gamma}_b^*/\dot{\gamma}_s^{*' becomes more negative, the profile becomes concave, reproducing the convexity changes observed by Silbert *et al.* [4]. To make our analytical solutions of  $u^*(y^*)$  more practical, the relationship between  $\eta$ ,  $\dot{\gamma}_b^*$ , and  $\dot{\gamma}_s^{*' is desired and will be further pursued.$$$

## 5 Acknowledgements

The authors acknowledge the financial support from Ministry of Science and Technology of Taiwan under grants MOST-112-2221-E-002-137-MY3 and NSTC-112-2923-E-002-003.

## References

- [1] Y. Forterre, O. Pouliquen. Annu. Rev. Fluid Mech. **40**, 1-24 (2008). <https://doi.org/10.1146/annurev.fluid.40.111406.102142>
- [2] F. da Cruz, S. Emam, M. Prochnow, J.-N. Roux, F. Chevoir. Phys. Rev. E **72**, 021309 (2005). <https://doi.org/10.1103/PhysRevE.72.021309>
- [3] P. Jop, Y. Forterre, O. Pouliquen. J. Fluid Mech. **541**, 167-192 (2005). <https://doi.org/10.1017/S0022112005005987>
- [4] L. E. Silbert, J. W. Landry, G. S. Grest. Phys. Fluids **15**, 1-10 (2003). <https://doi.org/10.1063/1.1521719>
- [5] P. Jop, Y. Forterre, O. Pouliquen. Nature **441**, 727-730 (2006). <https://doi.org/10.1038/nature04801>
- [6] J. Goyon, A. Colin, G. Ovarlez, A. Ajdari, L. Bocquet. Nature **454**, 84-87 (2008). <https://doi.org/10.1038/nature07026>
- [7] O. Pouliquen, Y. Forterre. Phil. Trans. R. Soc. A **367**, 5091-5107 (2009). <https://doi.org/10.1098/rsta.2009.0171>
- [8] K. Kamrin, G. Koval. Phys. Rev. Lett. **108**, 178301 (2012). <https://doi.org/10.1103/PhysRevLett.108.178301>
- [9] M. Bouzid, M. Trulsson, P. Claudin, E. Clément, B. Andreotti. Phys. Rev. Lett. **111**, 238301 (2013). <https://doi.org/10.1103/PhysRevLett.111.238301>
- [10] D. L. Henann, K. Kamrin. Phys. Rev. Lett. **113**, 178001 (2014). <https://doi.org/10.1103/PhysRevLett.113.178001>
- [11] D. G. Schaeffer, T. Barker, D. Tsuji, P. Gremaud, M. Shearer, J. M. N. T. Gray. J. Fluid Mech. **874**, 926-951 (2019). <https://doi.org/10.1017/jfm.2019.476>
- [12] P. V. Dsouza, P. R. Nott. J. Fluid Mech. **888**, R3 (2020). <https://doi.org/10.1017/jfm.2020.62>
- [13] P. C. Johnson, P. R. Nott, R. Jackson. J. Fluid Mech. **210**, 501-535 (1990). <https://doi.org/10.1017/S0022112090001380>
- [14] J. S. Fannon, I. R. Moyles, A. C. Fowler. J. Fluid Mech. **864**, 1026-1057 (2019). <https://doi.org/10.1017/jfm.2019.43>
- [15] K.-L. Lee, F.-L. Yang. J. Fluid Mech. **806**, 234-253 (2016). <https://doi.org/10.1017/jfm.2016.590>
- [16] GDR MiDi. Eur. Phys. J. E **14**, 341-365 (2004). <https://doi.org/10.1140/epje/i2003-10153-0>
- [17] X. Jiang, T. Matsushima. J. Jpn. Soc. Civ. Eng. **74**, 393-402 (2018). <https://doi.org/10.2208/jscejam.74.I-393>
- [18] K. Kamrin, D. L. Henann. Soft Matter **11**, 179-185 (2015). <https://doi.org/10.1039/C4SM01838A>
- [19] M. Bouzid, M. Trulsson, A. Izzet, A. F. de Coulomb, P. Claudin, E. Clément, B. Andreotti. EPJ Web Conf. **140**, 11013 (2017). <https://doi.org/10.1051/epjconf/201714011013>
- [20] P. C. Johnson, R. Jackson. J. Fluid Mech. **176**, 67-93 (1987). <https://doi.org/10.1017/S0022112087000570>